Wall modeled large-eddy simulation of shock wave/turbulent boundary layer interaction with separation

By I. Bermejo-Moreno, J. Larsson† AND J. Bodart‡

1. Motivation and objectives

The objective of this work is to assess the ability of large-eddy simulations employing an equilibrium wall model to reproduce the flow features present in strong interactions between an oblique shock wave and the turbulent boundary layers of an internal (duct) flow leading to mean flow separation. Such interactions (denoted STBLI) are pertinent, among other applications, to supersonic flight propulsion and have been extensively studied experimentally (Green 1970; Dolling 2001; Dupont *et al.* 2005, 2006; Piponniau *et al.* 2009; Souverein *et al.* 2010; Helmer *et al.* 2012; Campo *et al.* 2012) and numerically (see, for example, Wu & Martin 2008; Edwards 2008; Priebe *et al.* 2009; Touber & Sandham 2009*a*,*b*; Hadjadj *et al.* 2010; Pirozzoli *et al.* 2010; Pirozzoli & Bernardini 2011; Priebe & Martin 2012; Morgan *et al.* 2013). Existing numerical simulations, however, are often performed at reduced Reynolds numbers and on simplified geometries that forgo the three-dimensionality of practical configurations. The study presented in this brief is part of a larger enterprise (see Bermejo-Moreno *et al.* 2014) whose novelty is in the use of a wall model in a large-eddy simulation setting (thus allowing matching of the experimental Reynolds numbers) and the inclusion of three-dimensional effects (by considering the duct sidewalls ignored in the majority of previous simulations).

We consider the experiments of an oblique shock wave impinging on a turbulent boundary layer at a Mach number of approximately 2.3 performed by Dupont *et al.* (2005, 2006), Piponniau *et al.* (2009), Piponniau (2009) and Souverein *et al.* (2010). These experiments were done for several shock intensities in the continuously operated supersonic wind tunnel at the Institut Universitaire des Systèmes Thermiques Industriels (IUSTI). The shock intensity is set by varying the deflection angle of a sharp-edge plate (shock generator) attached to the top wall of the wind tunnel. The shock generator spans the tunnel cross-section and is located in the free-stream. The strongest interaction case, corresponding to the largest deflection angle (9.5°) of the incident shock tested experimentally, will be considered in our simulations, as it resulted in the strongest mean flow reversal observed experimentally. These experiments have been used in previous computational studies for validation purposes, mainly focusing on a lower (8°) deflection angle with milder separation. Most of these prior computational studies considered spanwise periodicity and a lower Reynolds number than in the experiments, to reduce the computational cost of the DNS or wall-resolved LES (see, for example, Garnier *et al.* 2002; Touber & Sandham 2009*a*; Pirozzoli & Bernardini 2011; Morgan *et al.* 2013). However, Garnier (2009) performed Stimulated Detached Eddy Simulation (SDES) for the 9.5° shock deflection angle case, including the top and sidewalls of the wind tunnel in the computational domain.

† Department of Mechanical Engineering, University of Maryland
‡ Université de Toulouse, ISAE, France

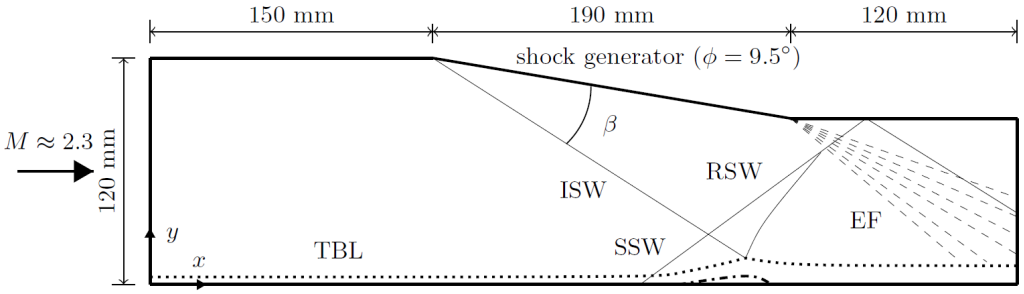

FIGURE 1. Side view (flow from left to right) of the computational domain including the shock generator (deflecting the free-stream an angle of $\phi = 9.5°$), and sketching the incident (ISW), reflected (RSW) and separated (SSW) shock waves, the expansion fan (EF) after the shock generator (dashed lines), the bottom-wall turbulent boundary layer (TBL, dotted line), and the separation bubble (dash-dotted line).

The sidewalls were found to strengthen the interaction, by reducing the effective section of the wind tunnel.

While it would be attractive to use existing (and more complete) DNS/LES numerical databases for validation purposes of the wall-modeling methodology, the low Reynolds numbers utilized in those simulations render any wall-modeled counterpart nearly irrelevant. As noted in Hutchins & Marusic (2007) and Pirozzoli (2012), the lowest Reynolds number that produces a logarithmic mean velocity behavior is $\mathrm{Re}_\tau \approx 670$. This poses a lower limit on the Reynolds number of flows for which wall-model simulations based on Prandtl's mixing length hypothesis (such as the formulation used in this study) are meaningful, since below that limit the mesh resolution requirements for the outer layer, particularly for the spanwise direction, become dominant, overcrossing the wall-resolved resolution requirements.

This brief is structured as follows. Section 2 presents the numerical methodology used in the simulations, describing the computational domain, mesh resolution, modeling approach, and boundary conditions. Results from the simulations are presented in Section 3, focusing first on global flow parameters of the incoming boundary layer and the separation bubble, followed by qualitative and quantitative comparisons of time-averaged flow quantities, the three-dimensionality of flow separation, and low-frequency unsteadiness. Conclusions are presented in Section 4.

2. Methodology

The computational domain comprises only a section of the wind tunnel containing the shock generator and the first STBLI on the bottom wall (see Figure 1). The full cross-section of the wind tunnel (120 mm tall in y and 170 mm wide in z) is considered so as to include the confinement effects imposed by the sidewalls. The shock generator is modeled as a 9.5° inclined compression on the top wall extending 190 mm downstream, and thus protruding into the free-stream, followed downstream by a constant area-section. Note that in the experiment, a sharp-edge plate was placed directly in the free-stream and attached to the top wall. The inlet of the computational domain is located 150 mm upstream of the start of the shock generator, whereas the outlet is located 310 mm downstream.

The spatially filtered compressible Navier-Stokes equations for the conserved vari-

ables of mass, momentum, and total energy of a calorically perfect gas are solved using a control volume-based discretization, finite volume formulation on unstructured hexahedral meshes with the code CharLES^x, developed at the Center for Turbulence Research. A non-dissipative centered numerical scheme is combined with an essentially non-oscillatory (ENO), second-order shock-capturing scheme (with an HLLC Riemann solver for the computation of inviscid fluxes). The shock-capturing scheme is applied in regions near shock waves, identified by a shock sensor activated according to the criterion: $-\partial u_k/\partial x_k > \max(\sqrt{\omega_j\omega_j}, 0.05c/\Delta)$, where $\partial u_k/\partial x_k$ is the local dilatation, $\omega_j\omega_j$ is the enstrophy, c is the sound speed and Δ is the mesh cell size. Subgrid-scale stresses are modeled following Vreman (2004), and the subgrid-scale heat flux is modeled using a fixed turbulent Prandtl number of 0.9. Subgrid-scale model terms are set to zero in regions where the shock-capturing scheme is active, to avoid adding extra dissipation to the ENO scheme (see Bermejo-Moreno *et al.* 2010). The discretized equations are advanced in time using a three-stage, third-order explicit Runge-Kutta algorithm.

Synthetic turbulence is generated at the inflow plane using the digital filtering technique of Touber & Sandham (2009*b*) (based on earlier work by Klein *et al.* 2003; Xie & Castro 2008), from experimental PIV measurements of mean and turbulence quantities taken at the spanwise-center plane (Piponniau 2009) near the bottom wall. Since no experimental PIV data were reported in planes away from the spanwise center of the duct, the one-dimensional PIV profiles extracted at the center plane are extruded along the spanwise direction up to a distance to each sidewall equal to the bottom wall boundary layer thickness, and translating the relevant information needed to complete the mean and turbulence wall-normal profiles in the sidewall boundary layers from the bottom wall boundary layer. The thicknesses of the sidewalls and bottom wall boundary layers are thus assumed equal. While this characterization of the sidewall boundary layers is far from complete, the effect of confinement is at least present in these simulations. The digital filtering technique employs mean velocities, single-point correlations specified and two-point correlations characterized through integral lengthscales in each coordinate direction: presently, we consider a lengthscale of the order of the incoming boundary layer thickness, δ_o, in the streamwise direction (based on Pirozzoli 2012, and references therein), and half that lengthscale in the transverse directions (y and z).

The equilibrium wall model described in Kawai & Larsson (2012) is applied on the bottom wall, considered adiabatic. The wall model solves the equilibrium-boundary-layer equations in a refined, near-wall inner grid, embedded in the coarser, background LES grid

$$\frac{\mathrm{d}}{\mathrm{d}\eta}\left[(\mu+\mu_t)\,\frac{\mathrm{d}u_\parallel}{\mathrm{d}\eta}\right]=0, \tag{2.1}$$

$$\frac{\mathrm{d}}{\mathrm{d}\eta}\left[(\mu+\mu_t)\,u_\parallel\frac{\mathrm{d}u_\parallel}{\mathrm{d}\eta}+c_p\left(\frac{\mu}{\mathrm{Pr}}+\frac{\mu_t}{\mathrm{Pr}_t}\right)\frac{\mathrm{d}T}{\mathrm{d}\eta}\right]=0, \tag{2.2}$$

where $u_\parallel$ is the wall-parallel velocity, T is the temperature, c_p is the fluid-specific heat capacity at constant pressure, μ is the fluid molecular viscosity, Pr is the Prandtl number, and μ_t is the wall-model eddy-viscosity, which is taken from a mixing-length model as

$$\mu_t=\kappa\rho\eta\sqrt{\tau_w/\rho}\left[1-\exp\left(-\frac{\eta^+}{A^+}\right)\right]^2. \tag{2.3}$$

The model parameters are set constant: $\kappa=0.41$, $\mathrm{Pr}_t=0.9$, $A^+=17$. The inner, wall-model simulation takes the LES flow variables $(\rho, u_\parallel, T)$ as the outer boundary

condition at a specified wall-normal distance, h_{wm}. After the system of ODEs (2.1)-(2.2) is solved, the LES takes from the wall-model inner simulation the wall shear stress (τ_w) and temperature (T_w) or heat-flux (q_w), for an adiabatic or isothermal boundary condition, respectively.

Since data of the incoming boundary layers on the side and top walls were not reported experimentally, no-slip adiabatic boundary conditions are used in the simulations, with the aim to assess any confinement effects, but not to have a full characterization of the flow features near those walls. Simulations with and without sidewalls (i.e., spanwise periodic) are performed in this work, and the results compared with experimental data. The width of the computational domain in the spanwise periodic simulations is $6\delta_o$, which reduces the computational cost of the simulation while still ensuring that it is sufficiently wide to avoid spurious effects on the size of the separation bubble (see Touber & Sandham 2009*b*; Morgan *et al.* 2013). Spanwise averaging is used in the spanwise periodic simulation.

A uniform mesh resolution is chosen in the streamwise and spanwise directions, equal to $\delta_o/\Delta_x \approx 8$ and $\delta_o/\Delta_z \approx 16$, respectively. The mesh spacing at the wall in the wall-normal direction is $\delta_o/\Delta_y \approx 40$, stretching to a uniform $\delta_o/\Delta_y \approx 10$ spacing above $3\delta_o$. In viscous units, $\Delta_x^+ \approx 100$, $\Delta_y^+ \approx 20 \rightarrow 80$ and $\Delta_z^+ \approx 50$. The exchange location of the wall model, at which information from the LES outer grid is transferred to the wall-model inner grid as the free-stream boundary condition, is located $0.06\delta_o$ above the wall. Statistics are collected for approximately 85 flow-through times ($\approx 3500\delta_o/U_o$, where $U_o \approx 550$ m/s is the centerline velocity at the inflow).

3. Results

Flow parameters of the incoming boundary layer and the separation bubble at the interaction are presented in Table 1, comparing experiments (Piponniau *et al.* 2009; Souverein *et al.* 2010) and simulations. The interaction length, L_i, is defined as the distance between the mean position of the foot of the separation shock and the extrapolation to the bottom wall of the incident shock, taken as the origin of the streamwise coordinate, x.

Wall-resolved LES of this experiment, performed by Morgan *et al.* (2013) at a reduced Reynolds number of $\mathrm{Re}_\theta = 1500$, resulted in an interaction length of $L_i/\delta_o = 3.8$, lower than the $L_i/\delta_o = 4.5$ obtained in the present wall-modeled LES (WMLES) when spanwise periodicity is used. Note that those values are significantly lower than the $L_i/\delta_o = 6.4$ found in the WMLES with sidewalls, which is in close agreement with the 6.45 value reported in the experiments (Dupont *et al.* 2006). This result indicates that the underprediction of L_i found in existing DNS and LES of STBLI is likely dominated by the assumption of spanwise periodicity that prevents any confinement effects otherwise imposed by sidewalls. A lowered Reynolds number can lead to an underprediction of the interaction length in simulations, but its relevance may be smaller in the interaction length, as was suggested in the parametric study of Morgan *et al.* (2013) for a lower range of Reynolds numbers.

Despite the agreement in the interaction length between experiments and simulations with sidewalls, the separation length, L_s, and the maximum height of the dividing streamline, h, are underpredicted in the simulations. While these values are considerably improved with respect to spanwise periodic simulations, the underprediction is still significant (23% and 59%, respectively). One possible cause for this discrepancy might be the use of a wall model in the region of separated flow, that could be better modeled by

	M	δ_{99} (mm)	θ (mm)	H	Re_θ ($\times 10^3$)	C_f ($\times 10^{-3}$)	u_τ (m/s)	L_i (mm)	L_s (mm)	h (mm)	$\Delta p/2\tau_{w0}$
Experiment	2.28	11	0.96	3.53	5.1	2	$\approx$25	71.5	66.5	10.2	50
WMLES$_s$	2.27	11.5	0.99	3.54	5.5	2.1	23.8	70.0	51.1	4.2	48.6
WMLES$_p$	2.28	11.5	0.98	3.57	5.5	2.1	23.4	51.5	32.2	1.6	48.8

TABLE 1. Flow parameters from experiments (Piponniau *et al.* 2009; Souverein *et al.* 2010) and simulations (WMLES$_s$: simulation with sidewalls, WMLES$_p$: simulation with spanwise periodicity): M, free-stream Mach number; δ_{99}, boundary layer thickness; θ, momentum thickness; H, shape factor; Re_θ, Reynolds number based on the momentum thickness and the free-stream density, velocity and dynamic viscosity; C_f, streamwise skin friction coefficient (a value of 2.1×10^{-3} is reported in Souverein *et al.* 2010); u_τ, friction velocity; L_i, interaction length; L_s, separation length (difference between separation and reattachment points); h, maximum height of the mean dividing streamline line (defined as $y_d(x)$ such that $\int_0^{y_d(x)} \rho u dy = 0$); $\Delta p/2\tau_{w0}$, normalized shock intensity (Δp is the pressure jump across the incident shock and τ_{w0} is the wall shear stress of the incoming boundary layer).

locally reverting to a no-slip boundary condition (without a wall model), possibly owing to the reduced friction Reynolds number of the separated region. This approach would require the addition of a sensor to the flow solver capable of distinguishing attached and separated flow regions and selectively apply the wall model only in the former. Note, however, that regions with attached flow but at low-friction Reynolds number are still well characterized by the wall model, as the wall-model equations reproduce the mean velocity profile throughout the linear, buffer, and logarithmic layers. Other factors that might lead to discrepancies of the length and height of the separation bubble between experiments and present simulations are differences in the streamwise extent of the shock generator, whose geometry is not fully characterized in Piponniau *et al.* (2009), as well as different boundary layer thicknesses on the sidewalls (considered of equal thickness to that of the bottom wall in the present simulations, due to lack of PIV data away from the center plane).

Time-averaged mean streamwise velocity profiles on the center plane for the incoming boundary layer near the bottom wall upstream of the STBLI are presented in Figure 2(a) in outer and viscous units. A good agreement between experiments and simulations is seen. Note that only the simulation with sidewalls is considered in that figure. The downstream evolution of the wall pressure across the STBLI is shown in Figure 2(b). The simulation follows the experimental values except in the region near the separation point (indicated by the leftmost vertical dashed line), where it underpredicts the experimental values. This region partially overlaps with the oscillation zone of the unsteadiness of the separation shock. The variability in experimental measurements of wall pressure can be inferred from the upstream values included in Figure 2(b). The agreement between simulation and experiment improves halfway through the mean separation bubble, reaching a common value downstream of the interaction, significantly lower than the one corresponding to inviscid theory (indicated by a dash-dotted line).

Contours of time-averaged velocities and Reynolds stresses extracted from the vertical plane located at the spanwise center of the wind tunnel are shown in Figure 3. As in previous numerical studies (Pirozzoli & Bernardini 2011; Morgan *et al.* 2013), the

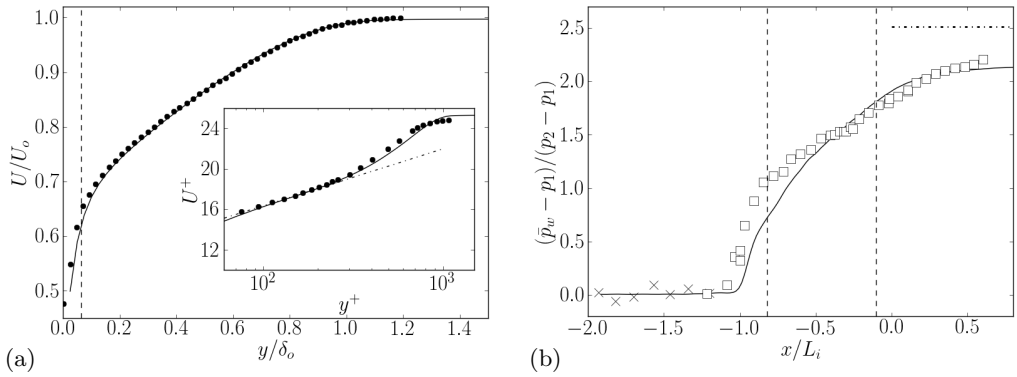

FIGURE 2. (a) Wall-normal profile of time-averaged mean streamwise velocity of the incoming boundary layer at the spanwise center, comparing WMLES$_s$ results (solid line) and experiment (symbols) (from Souverein *et al.* 2010). The vertical dashed line indicates the exchange location of the wall model. The inset shows the van Driest transformed streamwise velocity above the wall-model exchange location. (b) Streamwise profile of the time-averaged mean wall pressure, $\bar{p}_w$, along the STBLI (p_1 is the pressure upstream of the interaction, p_2 is the pressure downstream of the incident oblique shock), comparing WMLES$_s$ results (solid line) with experiments (symbols) (Dupont *et al.* 2006): squares correspond to $\theta = 9.5^\circ$; crosses correspond to $\theta = 7^\circ$ and are shown in this plot only upstream of the interaction, where experimental data for $\theta = 9.5^\circ$ were not available. Vertical dashed lines represent the separation and reattachment points found in the WMLES$_s$ based on the time-averaged mean velocity field. The horizontal dash-dotted line on the top left corresponds to the pressure downstream of the shock reflection resulting from inviscid theory ($(\bar{p}_{wi} - p_2)/(p_2 - p_1) \approx 2.51$).

coordinate axes have been rescaled with the interaction length, L_i. While this scaling has no effect on the comparison between experiments and results from the simulation with sidewalls (since the interaction lengths are practically the same, as shown in Table 1), the simulation with spanwise periodicity has a significantly shorter interaction length and thus this rescaling step was necessary in those prior studies for a meaningful comparison and is replicated here. Despite improved results derived from this rescaling step for the spanwise periodic simulation, the agreement of flow features between experiments and simulations is superior for the simulation with sidewalls. For example, the contour lines of streamwise velocity in the relaxation region depicted in Figure 3(a,f) follow more closely the experimental contours. Likewise, the height and shape of the region of high normal streamwise Reynolds stress shown in Figure 3(c,h) are better captured in the simulation with sidewalls.

A more quantitative comparison between experiments and simulations (with and without sidewalls) is presented in Figures 4 and 5 which show one-dimensional, wall-normal profiles at different streamwise locations in the interaction region and upstream. In these figures, the wall-normal coordinate has been rescaled with the interaction length, as was done in Figure 3. Good agreement is seen for time-averaged streamwise and vertical velocities for the simulation with sidewalls, with some discrepancies observed for profiles in the separated and relaxation regions, where the streamwise velocity is somewhat overpredicted near the wall. The experimental values of streamwise and shear Reynolds stresses are closely followed by the simulation results, as seen in Figure 5(a,c). Vertical Reynolds stresses from the simulations shown in Figure 5(b) appear to overpredict the experimental values, dropping more slowly to zero away from the wall. A region of high

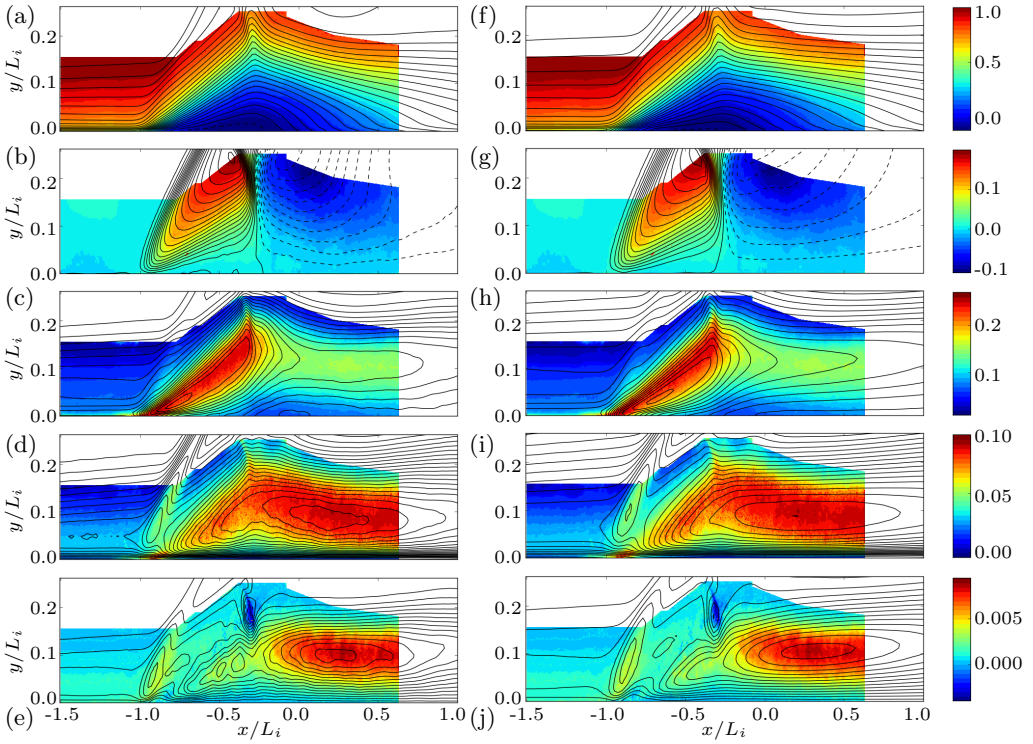

FIGURE 3. Time-averaged velocities and Reynolds stresses on the spanwise center plane in the STBLI region. Experimental PIV data (Piponniau *et al.* 2009; Piponniau 2009) shown as background colormaps, with simulation results given by (15) black contour lines superimposed. Left plots (a-e) correspond to the simulations with sidewalls, whereas right plots (f-j) correspond to spanwise-periodic simulations. From top to bottom: streamwise velocity, U/U_o (a,f); vertical velocity, V/U_o (b,g); streamwise normal Reynolds stress, $\sqrt{\overline{u'u'}}/U_o$ (c,h); vertical normal Reynolds stress, $\sqrt{\overline{v'v'}}/U_o$ (d,i); Reynolds shear stress, $-\overline{u'v'}/U_o^2$ (e,j).

vertical Reynolds stress seen experimentally at the foot of the separation shock is not captured in the simulations, as observed in Figures 5(b) and 3(d,i) at $x/L \approx -0.9$.

Two additional features of the interaction observed experimentally are explored in the simulations: flow three-dimensionality imposed by the sidewalls and low-frequency unsteadiness near the separation shock.

To study the three-dimensionality of the flow in the separated region, Figure 6 shows mean streamlines and separation lines on horizontal planes extracted at increasing heights from the bottom wall. Simulation results show qualitatively a similar three-dimensionality imposed by the sidewalls with respect to experimental PIV data (see Dussauge *et al.* 2006; Piponniau 2009): the separation bubble appears confined to a core region of the duct, with two counter-rotating vortices observed downstream of the separation shock ($x/L_i > -1$). The traces of these vortices are located approximately halfway along the interaction region very close to the bottom wall and move downstream and closer to the spanwise center plane for increasing height of the horizontal plane. These results are consistent with the experimental findings of Dussauge *et al.* (2006), who considered these tornado-like vortices responsible for unsteady shock motions. Despite the qualitative agreement, the core of these vortices at the bottom wall is closer to the centerplane in the experiments than in the simulations. The upstream shape of the separation bubble also appears to

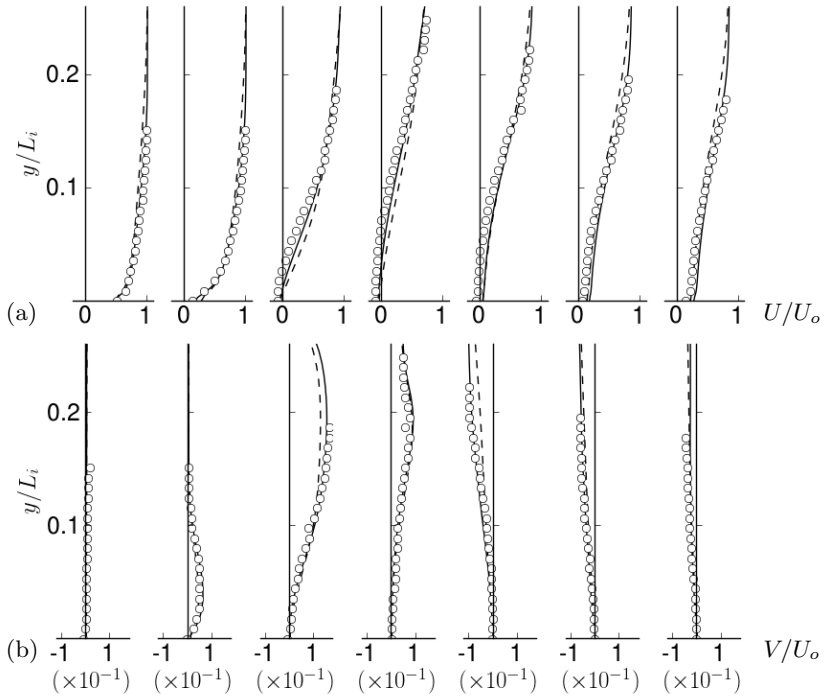

FIGURE 4. One-dimensional wall-normal profiles of time-averaged streamwise (a) and vertical (b) velocities, U/U_o and V/U_o, extracted at rescaled streamwise locations $x/L_i = \{-1.2, -0.9, -0.6, -0.3, 0.0, 0.3, 0.6\}$. Symbols: PIV experimental data (from Piponniau 2009); solid line: data from simulation with sidewalls; dashed line: data from simulation with spanwise periodicity.

differ, being more diamond-like in the experiments (see Figure 6 in Dussauge *et al.* 2006)), whereas the simulations show a region near the spanwise core of the duct that is more two-dimensional. The actual thickness of the sidewall boundary layers, not characterized in the experiment and likely different from our simulations, might be responsible for these discrepancies.

Contours of premultiplied power spectral density (PSD′) of wall pressure signals from the simulations are presented in Figure 7, showing evidence of the low-frequency unsteadiness also observed experimentally. Pressure signals are extracted from point probes located at the spanwise center along the bottom wall. The PSD′ is plotted as a function of the streamwise location and the normalized frequency $\mathrm{St} = f\delta_o/U_o$. The sampling frequency is $f \approx 200U_o/\delta_o$. The PSD′ at each streamwise location has been normalized with its integrated value across all frequencies. In agreement with previous studies (for a review, see Clemens & Narayanaswamy 2014), three distinct zones can be seen in Figure 7: first, upstream of the interaction ($x/L < -1$) energy is contained in frequencies of the order of the characteristic boundary layer frequency ($\mathrm{St} = O(1)$); second, at the start of the interaction region ($x/L \approx -1$), near the foot of the separation shock, the pressure signal shows the dominance of low frequencies such that $\mathrm{St} = O(0.01)$; third, farther downstream in the interaction region, the low frequencies are no longer dominant, but intermediate frequencies develop, and the original dominant frequencies of the incoming boundary layer appear progressively lowered by the action of the STBLI. Note that in

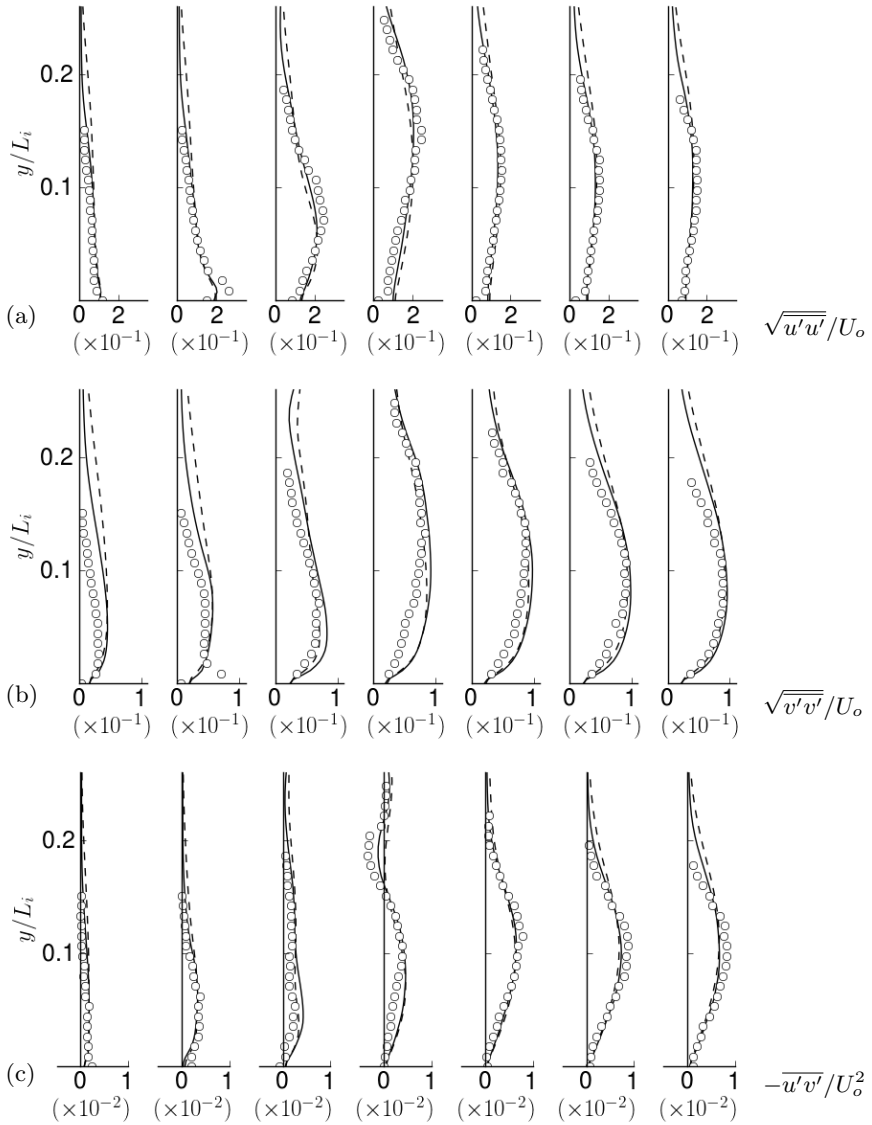

FIGURE 5. One-dimensional wall-normal profiles of time-averaged Reynolds stresses extracted at rescaled streamwise locations $x/L_i = \{-1.2, -0.9, -0.6, -0.3, 0.0, 0.3, 0.6\}$. (a) Streamwise Reynolds stress, $\sqrt{\overline{u'u'}}/U_o$; (b) Vertical Reynolds stress, $\sqrt{\overline{v'v'}}/U_o$; (c) Reynolds shear stress, $-\overline{u'v'}/U_o^2$. Symbols: PIV experimental data (from Piponniau 2009); solid line: data from simulation with sidewalls; dashed line: data from simulation with spanwise periodicity.

the relaxation region ($x/L_i > 0$), higher frequencies observed in the incoming boundary layer are recovered and amplified, while the rest of the spectral density function has been broadened with respect to the incoming boundary.

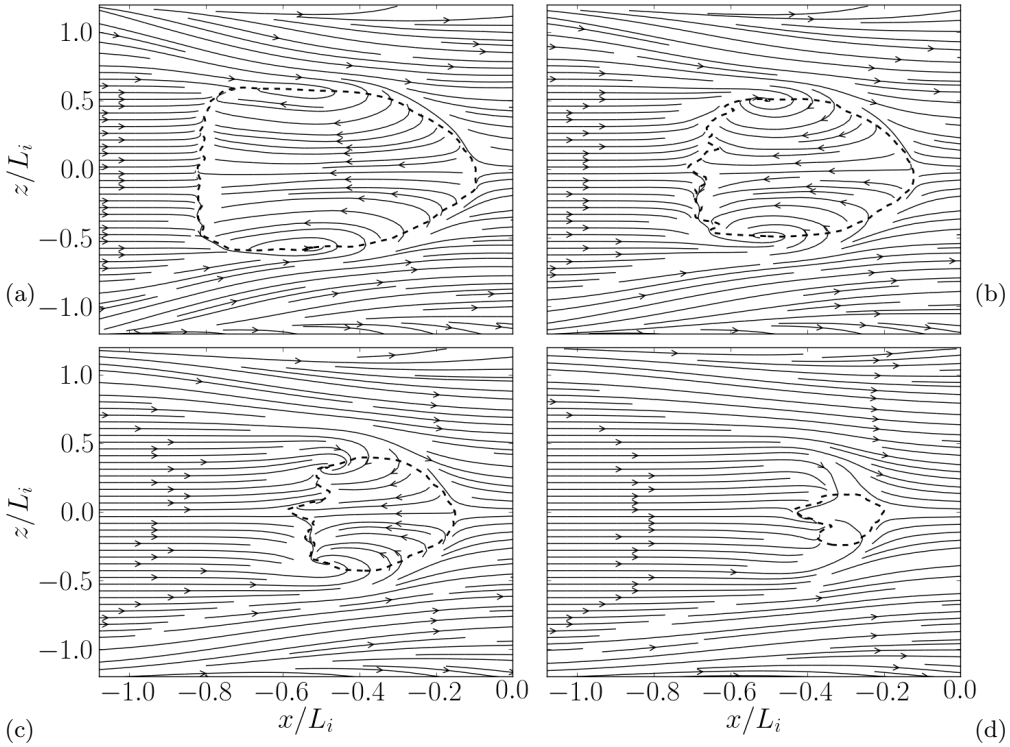

FIGURE 6. Streamlines (solid lines with arrows indicating the fluid motion) obtained from time-averaged mean velocity on horizontal planes extracted at $y/h = \{0.02, 0.12, 0.24, 0.48\}$ locations (a, b, c, d, respectively). Dashed lines represent the loci of mean longitudinal velocity, thus demarcating the separation bubble.

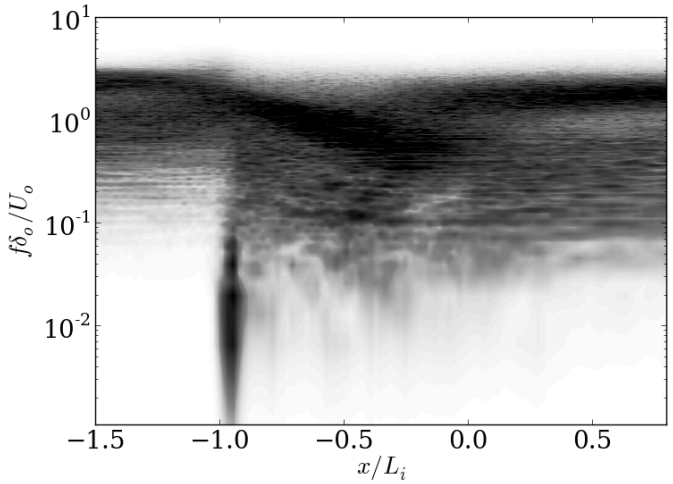

FIGURE 7. Contours of premultiplied power spectral density (PSD′) (arbitrary scale) of wall pressure signals on the bottom wall at the spanwise center of the duct, as a function of the streamwise location (rescaled by the interaction length, L_i) and the Strouhal number $\mathrm{St} = f\delta_o/U_o$. PSD′s are normalized for each streamwise location.

4. Conclusions

We have presented wall-modeled large-eddy simulations of the interaction between a shock wave and the turbulent boundary layers inside a supersonic duct flow, replicating the experiment of Dupont *et al.* (2005, 2006), Piponniau *et al.* (2009) and Souverein *et al.* (2010) for the stronger interaction case ($M \approx 2.3$, with a deflection angle of 9.5°), which results in mean flow reversal. The use of a wall model allowed us to reach the experimental Reynolds number and include the full spanwise duct geometry at a feasible computational cost. Simulations with and without duct sidewalls were performed to assess the influence of three-dimensional confinement effects on the interaction.

Most global flow parameters are well reproduced by the simulation including sidewalls, with the exception of the size of the separation bubble, which is underpredicted with respect to the experiments (particularly its maximum height), even though the interaction length is well matched. The qualitative and quantitative agreement of flow features, location, and extent of the extrema of time-averaged flow quantities appears reasonably good. In contrast, the simulation without sidewalls (spanwise periodic) presents a much smaller separation bubble and an underprediction of the interaction length, requiring a rescaling of the coordinate system for a meaningful comparison of flow features with the experiment. Such underprediction of the interaction length for the spanwise periodic simulation, and the subsequent rescaling step, is common to previous numerical simulations that also assumed spanwise periodicity and is indicative of the importance of three-dimensional effects of confinement imposed by the sidewalls for a correct characterization of the interaction. Thus, a more complete characterization of the flow field near the side walls of the duct (in addition to the center plane) in the experiments appears necessary to assess those three-dimensional effects as well as to properly set up the simulations for comparison.

Further insight into the three-dimensionality of this flow is provided in the simulation results by confirming the presence of tornado-like vortices on the lateral edges of the separation bubble, consistent with earlier experimental findings. Finally, a frequency analysis of the wall pressure time signal reveals the existence of low-frequency ($St = O(0.01)$) motions near the foot of the separation shock, also observed experimentally.

Acknowledgments

Financial support was provided by the United States National Nuclear Security Administration of the Department of Energy under the Predictive Science Academic Alliance Program (PSAAP) at Stanford University (DE-FC52-08NA28614). Computer time was provided by the Open Computing Facility (OCF) at Lawrence Livermore National Laboratory (LLNL), and the High Performance Computing Center at Stanford University (NSF MRI-R2 award 960306).

REFERENCES

Bermejo-Moreno, I., Campo, L., Larsson, J., Bodart, J., Helmer, D. & Eaton, J. K. 2014 Confinement effects in shock wave/turbulent boundary layer interactions through wall-modeled large-eddy simulations. *J. Fluid Mech.* **758**, 5–62.

Bermejo-Moreno, I., Larsson, J. & Lele, S. K. 2010 LES of canonical shock-turbulence interaction. *Annual Research Briefs*, Center for Turbulence Research, Stanford University, pp. 209–222.

Campo, L. M., Helmer, D. B. & Eaton, J. K. 2012 Validation experiment for shock boundary layer interactions: sensitivity to upstream geometric perturbations. In *53rd Structures, Structural Dynamics and Materials Conference.*

Clemens, N. T. & Narayanaswamy, V. 2014 Low-frequency unsteadiness of shock wave/turbulent boundary layer interactions. *Annu. Rev. Fluid Mech.* **46**, 469–492.

Dolling, D. S. 2001 Fifty years of shock-wave/boundary-layer interaction research: what next? *AIAA J.* **39**, 1517–1531.

Dupont, P., Haddad, C., Ardissone, J. P. & Debiève, J. 2005 Space and time organization of a shock wave/turbulent boundary layer interaction. *Aerosp. Sci. Technol.* **9**, 561–572.

Dupont, P., Haddad, C. & Debiève, J. 2006 Space and time organization in a shock-induced separated boundary layer. *J. Fluid. Mech* **559**, 255–277.

Dussauge, J.-P., Dupont, P. & Debiève, J.-F. 2006 Unsteadiness in shock wave boundary layer interactions with separation. *Aerosp. Sci. Technol.* **10**, 85–91.

Edwards, J. R. 2008 Numerical simulations of shock/boundary layer interactions using time-dependent modeling techniques: a survey of recent results. *Prog. Aerosp. Sci.* **44**, 447–465.

Garnier, E. 2009 Stimulated Detached Eddy Simulation of three-dimensional shock/boundary layer interaction. *Shock Waves* **19**, 479–486.

Garnier, E., Sagaut, P. & Deville, M. 2002 Large eddy simulation of shock/boundary-layer interaction. *AIAA J.* **40**, 1935–1944.

Green, J. E. 1970 Reflexion of an oblique shock wave by a turbulent boundary layer. *J. Fluid Mech.* **40**, 81–95.

Hadjadj, A., Larsson, J., Morgan, B. E., Nichols, J. W. & Lele, S. K. 2010 Large-eddy simulation of shock/boundary-layer interaction. *Proceedings of the Summer Program*, Center for Turbulence Research, Stanford University, pp. 141–152.

Helmer, D., Campo, L. & Eaton, J. 2012 Three-dimensional features of a Mach 2.1 shock/boundary layer interaction. *Exp. Fluids* **53**, 1347–1368.

Hutchins, N. & Marusic, I. 2007 Evidence of very long meandering features in the logarithmic region of turbulent boundary layers. *J. Fluid Mech.* **679**, 1–28.

Kawai, S. & Larsson, J. 2012 Wall-modeling in large eddy simulation: length scales, grid resolution and accuracy. *Phys. Fluids* **24**, 15105.

Klein, M., Sadiki, A. & Janicka, J. 2003 A digital filter based generation of inflow data for spatially developing direct numerical or large eddy simulations. *J. Comput. Phys.* **186**, 652–665.

Morgan, B., Duraisamy, K., Nguyen, N., Kawai, S. & Lele, S. K. 2013 Flow physics and RANS modelling of oblique shock/turbulent boundary layer interaction. *J. Fluid Mech.* **729**, 231–284.

Piponniau, S. 2009 *Instationnarités dans les décollements compressibles: cas des couches limites soumises à ondes de choc.* PhD Thesis, L'Univerisité de Provence.

Piponniau, S., Dussauge, J. P., Debiève, J. F. & Dupont, P. 2009 A simple model for low-frequency unsteadiness in shock-induced separation. *J. Fluid Mech.* **629**, 87–108.

Pirozzoli, S. 2012 On the size of the energy-containing eddies in the outer turbulent wall layer. *J. Fluid Mech.* **702**, 521–532.

Pirozzoli, S. & Bernardini, M. 2011 Direct numerical simulation database for impinging shock wave/turbulent boundary-layer interaction. *AIAA J.* **49**, 1307–1312.

Pirozzoli, S., Larsson, J., Nichols, J. W., Bernardini, M., Morgan, B. E. & Lele, S. K. 2010 Analysis of unsteady effects in shock/boundary layer interactions. *Annual Research Briefs*, Center for Turbulence Research, Stanford University, pp. 153–164.

Priebe, S. & Martin, M. P. 2012 Low-frequency unsteadiness in shock wave-turbulent boundary layer interaction. *J. Fluid Mech.* **699**, 1–49.

Priebe, S., Wu, M. & Martin, M. P. 2009 Direct numerical simulation of a reflected-shock-wave/turbulent-boundary-layer interaction. *AIAA J.* **47**, 1173–1185.

Souverein, L., Dupont, P., Debieve, J., van Dussaugen, J., Oudheusden, B. & Scarano, F. 2010 Effect of interaction strength on unsteadiness in turbulent shock-wave-induced separations. *AIAA J.* **48**, 1480–1493.

Touber, E. & Sandham, N. 2009*a* Comparison of three large-eddy simulations of shock-induced turbulent separation bubbles. *Shock Waves* **19**, 469–478.

Touber, E. & Sandham, N. 2009*b* Large-eddy simulation of low-frequency unsteadiness in a turbulent shock-induced separation bubble. *Theor. Comp. Fluid Dyn.* **23**, 79–107.

Vreman, A. W. 2004 An eddy-viscosity subgrid-scale model for turbulent shear flow: Algebraic theory and applications. *Phys. Fluids* **16**, 3670–3681.

Wu, M. & Martin, M. P. 2008 Analysis of shock motion in shockwave and turbulent boundary layer interaction using direct numerical simulation data. *J. Fluid Mech.* **594**, 71–83.

Xie, Z.-T. & Castro, I. P. 2008 Efficient generation of inflow conditions for large eddy simulation of street-scale flows. *Flow Turbul. Combust.* **81**, 449–470.